RSC Advances

PAPER

View Article Online
View Journal | View Issue

Cite this: *RSC Adv.*, 2015, **5**, 7237

Multi-walled carbon nanotubes composited with nanomagnetite for anodes in lithium ion batteries

Xiaoyu Li,[a] Hongbo Gu,[c] Jiurong Liu,*[a] Huige Wei,[b] Song Qiu,[a] Ya Fu,[a] Hailong Lv,[a] Guixia Lu,[a] Yiran Wang[b] and Zhanhu Guo*[b]

Received 25th November 2014
Accepted 15th December 2014

DOI: 10.1039/c4ra15228j

www.rsc.org/advances

In this work, multi-walled carbon nanotube (MWNT) nanocomposites with homogenously anchored nanomagnetite of 10–20 nm prepared by a hydrothermal-annealing method have been demonstrated to serve as anode materials for lithium ion batteries (LIBs) with a specific capacity of 829 mA h g^{-1} after 50 cycles at a current density of 100 mA g^{-1} and a reversible capacity of 686 mA h g^{-1} at a current density of 200 mA g^{-1} for the nanocomposites with a weight ratio of 1 : 1, much larger than the specific capacity of 230 mA h g^{-1} after 50 cycles at a current density of 100 mA g^{-1} and a reversible capacity of 195 mA h g^{-1} at a current density of 200 mA g^{-1} for the MWNTs. The MWNTs in the nanocomposites could efficiently buffer the strain of volume change during lithiation/delithiation and greatly improve the electrical conductivity of the electrodes. The superior electrochemical performances of the Fe_3O_4/MWNTs were found to originate from the unique conductive network of the MWNTs in the nanocomposites as well as the high capacity from the nanomagnetite.

1. Introduction

Lithium ion batteries (LIBs) are becoming the most widely used energy resource in portable electronic devices due to their high energy density, fast charge–discharge rate, and excellent cycling performance. However, commercial graphene anode materials normally have low theoretical capacity (372 mA h g^{-1}), which severely limits the application of LIBs in electric vehicles and hybrid electric vehicles.[1,2] Great efforts have been made to explore anode materials with high reversible capacity for LIBs. Recently, transition metal oxides, including Co_3O_4,[3] Fe_3O_4,[4] NiO,[5,6] CuO,[7] Mn_2O_3,[8,9] Cr_2O_3,[10–12] *etc.* have drawn growing attention to serve as anode materials due to their high theoretical capacity based on a unique conversion reaction with the formation of Li_2O during the discharge/charge processes.[13] Among the aforementioned transition mental oxides, Fe_3O_4 has been regarded as one of the most promising anode materials for LIBs owing to its high theoretical specific capacity (925 mA h g^{-1}), natural abundance and environmental benignity. However, similar to other metal oxides, Fe_3O_4 anode materials suffer from poor cycling performance due to large volume shrinkage/expansion during the charge/discharge processes, and low rate performance arising from the kinetic limitations, which severely restrict their applications.[14–17] Generally, anode materials with high specific capacity tend to sustain considerable amount of volume changes during the lithiation/delithiation processes, which result in pulverization of the active materials and disintegration of electrode.[18–20] Recently, attempts have been made to deal with the volume change to improve the cycling performance of metal oxide anodes, such as minimizing the particle size[21–24] or incorporating inert buffers to alleviate the fracture and pulverization of the electrode.[15,25–28]

Carbon nanotubes (CNTs) have attracted wide attentions as additives in constructing hybrid nanocomposites due to their superior electrical conductivity, high surface-to-volume ratio, ultrathin walls, and structural flexibility.[29,30] Their large specific surface area ensures high contact area between electrolyte and electrode, and the ultrathin walls shorten the Li-ion diffusion distance. In addition, CNTs can be well connected to form unique conductive networks to provide continuous conductive pathways for electron transport.[31] The CNTs can serve as not only conducting materials, but also an excellent inert confining buffer to accommodate the strain of volume change during the rapid charge/discharge processes.[32,33] Therefore, enhanced electrode performance can be achieved through the application of these unique electrode structures by incorporating transition metal oxides with CNTs. The combination of conductive network of CNTs and high capacity of Fe_3O_4 nanoparticles is a promising way to make anode materials with excellent electrode performance.[34–38] The Fe_3O_4/CNTs nanocomposites have

[a]*Key Laboratory for Liquid–Solid Structural Evolution and Processing of Materials, Ministry of Education and School of Materials Science and Engineering, Shandong University, Jinan, Shandong 250061, People's Republic of China. E-mail: jrliu@sdu.edu.cn*

[b]*Integrated Composites Lab (ICL), Dan F. Smith Department of Chemical Engineering, Lamar University, Beaumont, TX 77710, USA. E-mail: zhanhu.guo@lamar.edu; zguo10@utk.edu*

[c]*Department of Chemistry, Tongji University, Shanghai, 200092, People's Republic of China*

some potential applications in biomedicine, magnetic data storage, supercapacitor and fuel cell.[39–45] For example, He *et al.*[46] reported a method using polyvinyl alcohol (PVA) as a hydrogen bond functionalizing agent to modify CNTs to synthesize CNTs/Fe_3O_4 nanocomposites (656 mA h g^{-1} at a current density of 100 mA g^{-1}) applied as anode materials for LIBs. Guo *et al.*[47] synthesized Fe_3O_4–CNTs nanocomposites (702 mA h g^{-1} at a current density of 50 mA g^{-1} after 50 cycles) for application in LIBs by using $Sn(OH)_6^{2-}$ as inorganic dispersant. However, the electrode performances of Fe_3O_4/CNTs nanocomposites prepared by these methods need to be improved greatly to meet the demand of higher capacity and faster charge–discharge rate for current LIBs with larger scope of application.

In this paper, a novel hydrothermal method in methanol–glycerol solvent followed by an annealing process in argon atmosphere was used to prepare Fe_3O_4/multi-walled carbon nanotubes (MWNTs) nanocomposites. The X-ray diffraction (XRD), scanning electron microscope (SEM), transmission electron microscopy (TEM) are used to characterize the structure and morphologies of the obtained Fe_3O_4/MWNTs nanocomposites. X-ray photoelectron spectroscopy (XPS) is carried out to determine the elemental composition. Thermogravimetric analysis (TGA) and differential scanning calorimetry (DSC) are used for weight percentage determination and thermal property investigation. The electrochemical performances of the prepared Fe_3O_4/MWNTs nanocomposites as anode materials for LIBs are evaluated by cyclic voltammogram (CV), galvanostatic charge–discharge and electrochemical impedance spectroscopy (EIS) measurement techniques.

2. Experimental

2.1. Materials

Iron chloride hexahydrate ($FeCl_3 \cdot 6H_2O$), sodium hydroxide (NaOH), methanol (CH_3OH), glycerol ($C_3H_8O_3$), PVDF (C_5H_9NO, 99.0%), *N*-methyl-2-pyrrolidone (NMP) and concentrated nitric acid (65–68%) were purchased from Sinopharm Chemical Reagent Co., Ltd, China. The MWNTs (20–50 nm in diameter) were purchased from Shenzhen Nanotech Port Co., Ltd, China. Carbon black, Li foil and Celgard 2300 were purchased from Hefei Kejing Material Technology Co., Ltd, China. LiPF6 (dissolved in ethylene carbonate, dimethyl carbonate, and ethylene methyl carbonate with a volume ratio of 1 : 1 : 1) was purchased from Shenzhen Biyuan Technology Co., Ltd, China. All the chemicals were analytical grades and used as received without any further purification.

2.2. Preparation of acid-treated MWNTs

The purchased MWNTs were treated in concentrated nitric acid (65–68%) at 140 °C for 6 hours in a Teflon-lined stainless steel autoclave. After that, the acid-treated MWNTs were centrifuged and washed with deionized water and ethanol until the pH value of filtrate was around 7, then dried in vacuum for 24 hours.

2.3. Synthesis of Fe_3O_4/MWNTs nanocomposites with different weight ratios

The Fe_3O_4/MWNTs nanocomposites were synthesized as follows. The acid-treated MWNTs (0.1 g) were dispersed in a mixed solution of glycerol (10 mL) and methanol (15 mL) at room temperature for one-hour sonication, in which 0.4 g $FeCl_3 \cdot 6H_2O$ was dissolved under the magnetic stirring for 30 min. 25 mL 0.5 mol L^{-1} NaOH methanol solution was slowly added into the above solution and stirred for additional 30 min. After that, the solution was sealed in a Teflon-lined stainless autoclave and maintained at 200 °C for 12 h. After reaction, the product was centrifuged and washed with methanol for 5 times. The obtained powders were dried in vacuum at 60 °C for 12 h. In order to obtain highly crystallized structure of Fe_3O_4 nanoparticles, the black product was treated at 500 °C for 2 h under argon atmosphere with a heating rate of 2 °C min^{-1} in a quartz tube furnace. The weight ratio of Fe_3O_4 and MWNTs in these nanocomposites was estimated to be 1 : 1 (indexed as Fe_3O_4–MWNTs (1 : 1)). The Fe_3O_4/MWNTs nanocomposites with a Fe_3O_4–MWNTs weight ratio of 1 : 3 were prepared following the same procedures for comparison (indexed as Fe_3O_4–MWNTs (1 : 3)).

2.4. Characterizations

The crystal structure of the obtained products was determined by a Rigaku D/Max-RC X-ray diffractometer with Ni filtered Cu Kα radiation ($\lambda = 0.1542$ nm, $V = 40$ kV, $I = 50$ mA) in the range of 10–90° at a scanning rate of 4 °C min^{-1}. The morphology and microstructure of the products were observed by a JSM-6700F field emission scanning electron microscopy (SEM, accelerating voltage of 20 kV and electric current of 1.0×10^{-10} A), and a JEOL JEM-2100 transmission electron microscopy (TEM, accelerating voltage of 200 kV). X-ray photoelectron spectroscopy (XPS) was recorded by a Kratos Analytical spectrometer using Al Kα ($h\nu = 1486.6$ eV) radiation as the excitation source under an anode voltage of 12 kV and an emission current of 10 mA. To evaluate the content of MWNTs in the nanocomposites, TGA measurements were performed on a SDT thermal-microbalance apparatus from room temperature (about 20 °C) to 800 °C in air condition at a heating rate of 10 °C min^{-1}.

2.5. Electrochemical measurements

The anode electrodes were prepared as follows. Briefly, the active material, carbon black, and polyvinylidene fluoride (PVDF) were mixed at a weight ratio of 8 : 1 : 1 in *N*-methyl-2-pyrrolidinone (NMP) to form homogenous slurry. Then the slurry was deposited onto a copper foil substrate by the doctor-blade process followed by drying in vacuum at 120 °C for 12 h. And then the circular electrodes were punched out with a diameter of 14 mm. The CR2025-type cells were assembled using Li foil as counter and reference electrode, Celgard 2300 as separator, and 1.0 M LiPF6 (dissolved in ethylene carbonate, dimethyl carbonate, and ethylene methyl carbonate with a volume ratio of 1 : 1 : 1) as the

electrolyte. The assembly was performed in an argon filled glove-box.

The galvanostatic charge–discharge cycles were recorded in a voltage range of 0.02 to 3 V at various current densities on a LAND CT2001A battery test system (Wuhan Lanhe Co., Ltd). The CV experiment was performed on an IviumStat electrochemistry work station with a scanning rate of 0.3 mV s^{-1} and the potential *vs.* Li/Li^+ ranging from 0.01 to 3 V. The EIS was tested on the same instrument with an AC signal amplitude of 10 mV in a frequency range from 100 kHz to 0.01 Hz. The data were adopted to draw Nyquist plots using real part Z' as *X*-axis, and imaginary part Z'' as *Y*-axis.

3. Results and discussions

3.1. Characterizations of Fe_3O_4/MWNTs nanocomposites

Fig. 1 shows the XRD patterns of pure MWNTs and the as-prepared nanocomposites. Pure MWNTs are observed to display a broad diffraction peak centered at $2\theta = 22°$, indicating the existence of amorphous carbon.[48] The sharp peak at 26° corresponds to the (0 0 2) plane of CNTs with layered and hexagonal structure.[49] The XRD patterns of the nanocomposites correspond to the diffraction peaks of carbon ($2\theta = 26°$) and Fe_3O_4 with spinel structure based on JCPDS file card no. 65-3107, indicating the prepared iron oxide is Fe_3O_4. The strong and sharp peaks of Fe_3O_4 suggest a high crystallinity of the as-prepared Fe_3O_4 nanoparticles.[50] The peak intensity of carbon ($2\theta = 26°$) in the Fe_3O_4–MWNTs (1 : 3) nanocomposites is much stronger than that in the Fe_3O_4–MWNTs (1 : 1) nanocomposites, which is in well agreement with the higher weight ratio of MWNTs in the Fe_3O_4–MWNTs (1 : 3).

Fig. 2a–f show the SEM and TEM images of the samples. The surface of pure MWNTs is very smooth, Fig. 2a and b. Fig. 2c–f shows the SEM and TEM images of the Fe_3O_4–MWNTs (1 : 1). The TEM image of the Fe_3O_4–MWNTs (1 : 1) nanocomposites, Fig. 2d, clearly shows the presence of Fe_3O_4 nanoparticles on the surface of MWNTs. A uniform distribution of Fe_3O_4 nanoparticles with size of *ca.*10–20 nm is observed on the surface of MWNTs, Fig. 2e. The small size of nanoparticles can facilitate the ions diffusion and the conductive network of MWNTs can accommodate large volume change and improve the electrical conductivity of the nanocomposites. Fig. 2f is a high resolution TEM (HRTEM) image of the Fe_3O_4/MWNTs nanocomposites, clearly demonstrating the Fe_3O_4 nanoparticles and the wall of MWNTs. There exists a clear boundary between the Fe_3O_4 nanocrystals and the MWNTs. The lattice distance of 0.338 nm corresponds to the (0 0 2) plane of graphitic carbon. The measured lattice distance for the Fe_3O_4 nanoparticles is around 0.257 nm, corresponding to the (3 1 1) plane of Fe_3O_4. The observed clear lattice fringe of Fe_3O_4 nanoparticles indicates a high crystalline structure of the as-prepared Fe_3O_4 nanoparticles.[51]

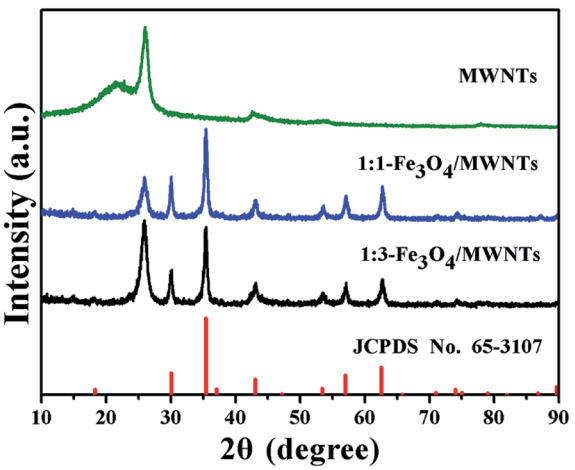

Fig. 1 XRD patterns of MWNTs, Fe_3O_4–MWNTs (1 : 1) and Fe_3O_4–MWNTs (1 : 3).

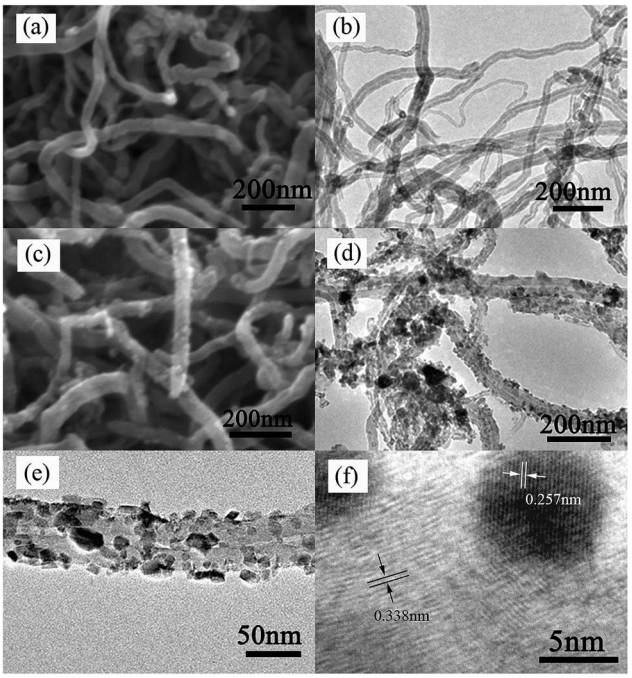

Fig. 2 (a) SEM image of MWNTs, (b) TEM image of MWNTs; and (c) SEM image of Fe_3O_4–MWNTs (1 : 1); (d–f) TEM images of Fe_3O_4–MWNTs (1 : 1).

The elemental composition of Fe_3O_4–MWNTs (1 : 1) was further investigated using XPS. The observed peaks of Fe2p, O1s, C1s in the survey scan XPS spectrum, Fig. 3a, indicate the existence of Fe, O and C elements in the as-prepared Fe_3O_4/MWNTs nanocomposites. Deconvolution of the C1s peak in the high resolution XPS spectrum, Fig. 3b, reveals three types of carbon bonds: C–C (284.6 eV), C–O–Fe (285.4 eV), and C═O (286.1 eV).[31,52] The formation of C–O–Fe bond indicates the intimate attachment of the Fe_3O_4 nanoparticles on the walls of MWNTs.[52] In the Fe2p spectrum (Fig. 3c), the peaks at 710.2 and 723.8 eV correspond to $Fe2p_{3/2}$ and $Fe2p_{1/2}$, respectively, which are in agreement with the XPS of Fe_3O_4 in the previous report.[53] The O1s spectrum (Fig. 3d) can be deconvoluted into three peaks, indicating three different oxygen species existed. The peak at 529.9 eV is due to the O–Fe of Fe_3O_4. The peak at

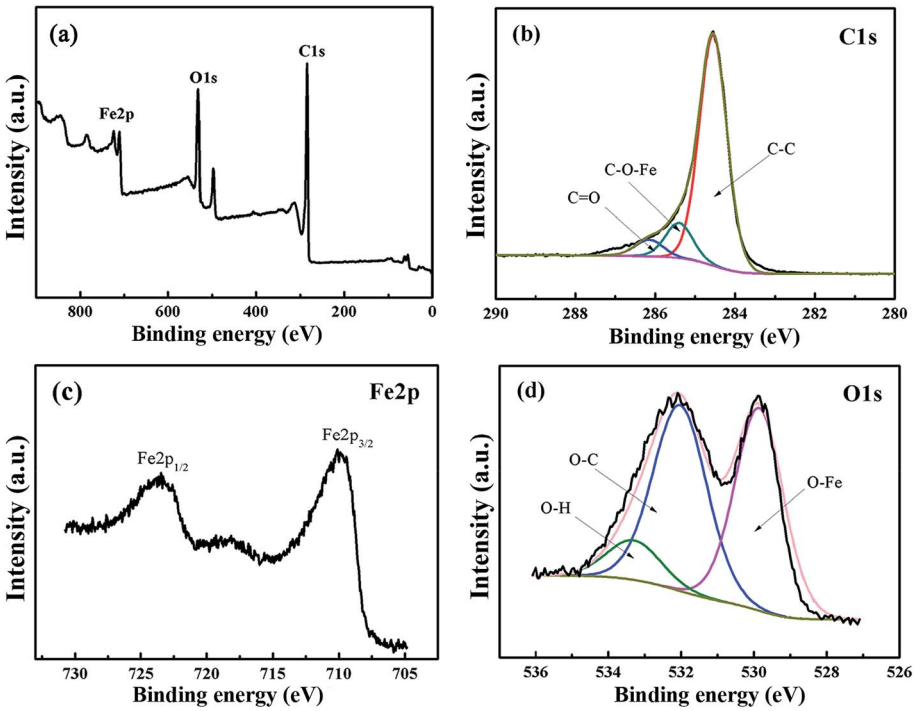

Fig. 3 XPS spectra of Fe_3O_4–MWNTs (1 : 1): (a) survey scan, (b) C1s, (c) Fe2p and (d) O1s.

532.0 eV can be attributed to the C–O bonds due to the surface oxidation of the MWNTs. The peak at 533.3 eV is assigned to the OH groups, arising from the moisture absorbed on the surface of the nanocomposites. The bond formation between MWNTs and Fe_3O_4 nanoparticles can not only accelerate the electron transfer but also stabilize the structure of nanocomposites during the charge/discharge process. According to the above analysis, the proposed formation mechanism of the prepared Fe_3O_4/MWNTs nanocomposites is given in Fig. 4.

To evaluate the content of MWNTs in the Fe_3O_4/MWNTs nanocomposites, TGA measurements were carried out in air up to 800 °C. The weight loss of 3.07 and 4.69% occurred separately in the Fe_3O_4–MWNTs (1 : 1) nanocomposites, Fig. 5a and Fe_3O_4–MWNTs (1 : 3) nanocomposites, Fig. 5b, between 20 and 170 °C, corresponding to the evaporation of water absorbed on the sample surface,[4] which is consistent with the analysis of XPS. From 350 to 600 °C, the observed sharp exothermic peak, along with the intensive weight loss of 49.19% in the Fe_3O_4–MWNTs (1 : 1) nanocomposites and the weight loss of 77.02% in the Fe_3O_4–MWNTs (1 : 3) nanocomposites are attributed to the degradation of MWNTs.[15] After 600 °C, no observed apparent exothermal peak or weight loss suggests the complete oxidation of the nanocomposites. The TGA results confirm that the MWNTs contents in the samples are in perfect accordance with the predetermined values before preparation.

3.2. Electrochemical performances of Fe_3O_4/MWNTs nanocomposites

The electrochemical performances of the prepared Fe_3O_4/MWNTs nanocomposites for LIBs were evaluated by galvanostatic charge–discharge, CV and EIS. Fig. 6a shows the selected discharge/charge voltage profiles of the Fe_3O_4–MWNTs (1 : 1) nanocomposite electrode between 0.01 and 3 V at a current density of 100 mA g^{-1}. There is a short voltage plateau around 1.0 V in the first discharge curve (Fig. 6a), corresponding the decomposition of electrolyte and the formation of solid electrolyte interphase (SEI) layer.[48,53–55] The voltage decrease to 0.75 V refers to the formation of $Li_xFe_3O_4$, and the voltage plateau at 0.75 V suggests the reduction of Fe^{3+} and Fe^{2+} to Fe^0 and the formation of amorphous Li_2O.[54,56] With the voltage drop to 0.02 V, the first discharge cycle delivers a total capacity of 1184 mA h g^{-1}, much higher than the theoretical capacity of

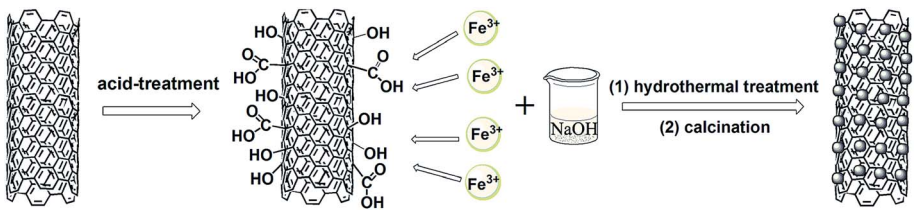

Fig. 4 The proposed formation mechanism of Fe_3O_4/MWNTs nanocomposites.

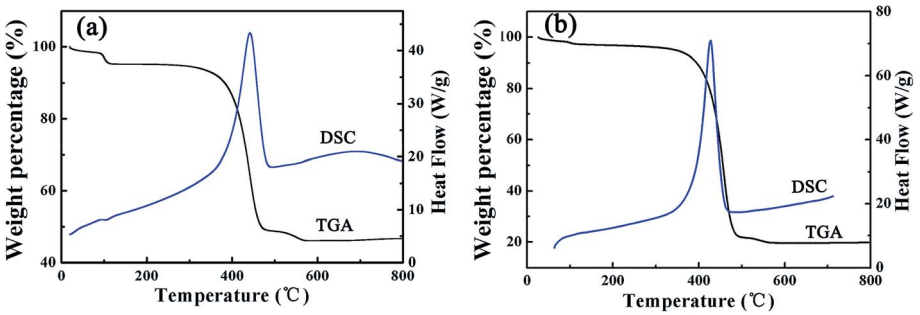

Fig. 5 TGA/DSC curves of (a) Fe_3O_4–MWNTs (1 : 1) and (b) Fe_3O_4–MWNTs (1 : 3) at a heating rate of 10 °C min^{-1} under air flux.

Fe_3O_4 (925 mA h g^{-1}). The first charge profile shows a slope from 1.5 to 2.0 V, suggesting the oxidation of Fe^0 to Fe^{2+} and Fe^{3+}.[4] The electrode exhibits a higher irreversible capacity in the first cycle, attributed to the formation of the SEI, the insertion of lithium-ions into the MWNTs, and the irreversible reaction of lithium-ions with Fe_3O_4 nanoparticles.[3,4,57,58]

The CV profiles for the initial three cycles of the Fe_3O_4–MWNTs (1 : 1) nanocomposites are shown in Fig. 6b. The observed peaks at 0.6 and 0.9 V in the first cathodic process are ascribed to the lithiation reaction of Fe_3O_4 to $Li_xFe_3O_4$ and $Li_xFe_3O_4 \rightarrow Fe^0 + Li_2O$,[55] electrolyte decomposition and SEI formation, respectively.[48,57,58] The peak at 0.9 V disappears in the subsequent cycles, in accordance with the aforementioned irreversible process. Meanwhile, two peaks at about 1.7 and 1.8 V in the anodic curve correspond to the oxidation of Fe^0 to Fe^{2+} and Fe^{3+} during the anodic process.[4] From the second cycle, both the cathodic peaks and the anodic peaks shift to higher potential positions, consistent with the results obtained from their discharge and charge curves. Similar peak shift towards high voltage has also been observed in other transition metal oxides, due to the polarization of active material in the first cycle.[59] There are no large position shift and intensity change for the main peaks in the 2nd and 3rd scans, indicating a good electrochemical reversibility of the Fe_3O_4/MWNTs electrode.

The electrochemical performances of the Fe_3O_4–MWNTs (1 : 3) nanocomposites and pure MWNTs electrode were also investigated under the same electrochemical conditions for comparison. Fig. 7a shows the cyclic performance of different electrodes at a current density of 100 mA g^{-1}. The Fe_3O_4–MWNTs (1 : 1) and Fe_3O_4–MWNTs (1 : 3) nanocomposite electrodes exhibit an initial specific capacity of 1184 and 782 mA h g^{-1}, which are stabilized to 829 mA h g^{-1} and 584 mA h g^{-1} after 50 cycles, respectively. It is observed that a stable reversible capacity of 230 mA h g^{-1} is observed for the pure MWNTs electrode within the cycling tests. These results demonstrate that the Fe_3O_4–MWNTs (1 : 1) nanocomposite electrode shows a better cycling performance than the Fe_3O_4–MWNTs (1 : 3) nanocomposite electrode. Theoretically, the capacity in these Fe_3O_4/MWNTs nanocomposites is mainly contributed by Fe_3O_4 due to the aforementioned low capacity of the MWNTs. The theoretical capacity can be estimated to be 648.5 mA h g^{-1} (= 925 mA h g^{-1} × 0.5 + 372 mA h g^{-1} × 0.5) for the Fe_3O_4–MWNTs (1 : 1) and 510.3 mA h g^{-1} (= 925 mA h g^{-1} × 0.25 + 372 mA h g^{-1} × 0.75) for the Fe_3O_4–MWNTs (1 : 3). Obviously, the obtained capacity is consistent with the theoretical expectations.

Fig. 7b shows the rate performances of the electrodes. The Fe_3O_4–MWNTs (1 : 3) nanocomposite electrode possesses a reversible capacity of 439, 414, 371, 280, 196 and 131 mA h g^{-1} at a current density of 100, 200, 400, 800, 1600 and 3200 mA g^{-1}, respectively. The Fe_3O_4–MWNTs (1 : 1) nanocomposite electrode markedly delivers higher reversible capacity of 714, 686, 624, 541, 408 and 294 mA h g^{-1} at the corresponding current densities, Fig. 7b. These results indicate that the Fe_3O_4–MWNTs (1 : 1) nanocomposite electrode demonstrates the best electrode performance among these three electrodes. It is noticed that

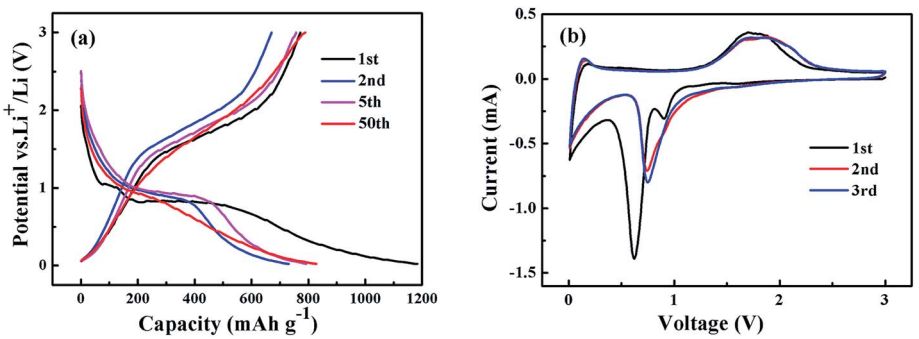

Fig. 6 (a) Galvanostatic discharge/charge curves of the 1st, 2nd, 5th and 50th cycles for Fe_3O_4–MWNTs (1 : 1) and (b) the CV curves of Fe_3O_4–MWNTs (1 : 1).

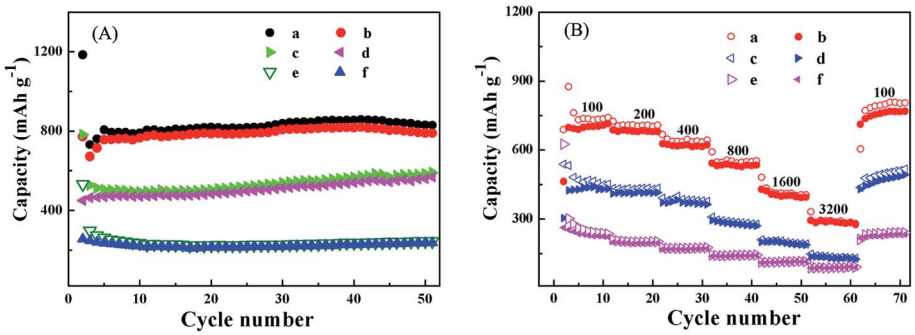

Fig. 7 (A) Cycling discharge performance for (a) Fe_3O_4–MWNTs (1 : 1), (c) Fe_3O_4–MWNTs (1 : 3) and (e) MWNTs, and charge performance for (b) Fe_3O_4–MWNTs (1 : 1), (d) Fe_3O_4–MWNTs (1 : 3) and (f) MWNTs at the current density of 100 mA g^{-1}. (B) Rate discharge performance for (a) Fe_3O_4–MWNTs (1 : 1), (c) Fe_3O_4–MWNTs (1 : 3) and (e) MWNTs and charge performance for (b) Fe_3O_4–MWNTs (1 : 1), (d) Fe_3O_4–MWNTs (1 : 3) and (f) MWNTs.

when the current density returns to 100 mA g^{-1} after the rate performance test, the discharge capacities of the Fe_3O_4–MWNTs (1 : 1) and Fe_3O_4–MWNTs (1 : 3) nanocomposites are 803 and 502 mA h g^{-1}, respectively, higher than those obtained at an initial density of 100 mA g^{-1}. Similar phenomena have also been found in other anode materials,[17,57] which were ascribed to the formation of polymer/gel-like films due to the decomposition of electrolyte driven by the active metal nanoparticles.[60–62] It also indicates that the integrity of the structure and the electrical contact are well maintained in the electrodes even under high charge/discharge rates. The fascinating electrochemical performance may originate from the unique architecture of the nanocomposites as well as the contribution of high capacity from the Fe_3O_4 nanoparticles. The electrode performance of the as-prepared Fe_3O_4/MWNTs nanocomposites is better than those of the reported CNTs-66.7 wt% Fe_3O_4 nanocomposite (656 mA h g^{-1} at a current density of 100 mA g^{-1}) synthesized through a method using polyvinyl alcohol (PVA) as a hydrogen bond functionalizing agent to modify multi-walled carbon nanotubes[46] and the reported 2 : 1 Fe_3O_4–CNTs electrode (702 mA h g^{-1} at a current density of 50 mA g^{-1} after 50 cycles) prepared by a inorganic dispersant assisted hydrothermal synthesis.[47]

To further investigate the electrochemical performances of the Fe_3O_4/MWNTs nanocomposites, EIS measurements, which were conducted on the samples fully-charged with an electrode potential of 3 V after 100 cycles at a current density of 100 mA g^{-1}, are shown in Fig. 8. The Nyquist plot of each sample is comprised of arc in the high-frequency region and the medium-frequency region, and an inclined line in the low frequency region. The diameter of the semicircle is in direct proportion to the impedance, which contains electrolyte resistance (R_e), surface film resistance (R_{sf}) and charge transfer resistance (R_{ct}).[43,54,63] The inclined line is assigned to the lithium-ion diffusion process inside the electrode materials corresponding to the Warburg impedance.[32,64] The impedance spectra can be fitted based on a reasonable equivalent circuit (inset of Fig. 8), in accordance with the physical mechanism of the Li-ion insertion/extraction for the electrodes. The fitted curves are in accord with the experimental data.[10,65] The (R_e + R_{sf} + R_{ct}) value for the Fe_3O_4–MWNTs (1 : 1) nanocomposites, Fe_3O_4–MWNTs (1 : 3) nanocomposites, and pure MWNTs is *ca.* 346, 207 and 61 Ω, respectively. It can be found that the R_{sf} and R_{ct} of the Fe_3O_4/MWNTs nanocomposite electrodes are distinctly decreased with increasing the weight ratio of MWNTs in the nanocomposites, indicating that the incorporation of MWNTs greatly enhances the charge transfer in the electrode. Moreover, as shown in Fig. 8, the Fe_3O_4–MWNTs (1 : 1) nanocomposites exhibit the smallest slope at low frequencies, indicating that the lithium ion diffusion in the electrode can be greatly improved with the incorporation of MWNTs.[4,42,66] The MWNTs in the nanocomposites can not only provide good electrode electron contact and electrical conductivity, but also facilitate the lithium ion diffusion.[64,67,68] All these contribute to the enhanced capacity of the Fe_3O_4/MWNTs nanocomposites.

From the above results and discussion, the superior electrochemical performance of the Fe_3O_4/MWNTs nanocomposites can be attributed to the following reasons. (1) The presence of MWNTs improves the electrical conductivity of the

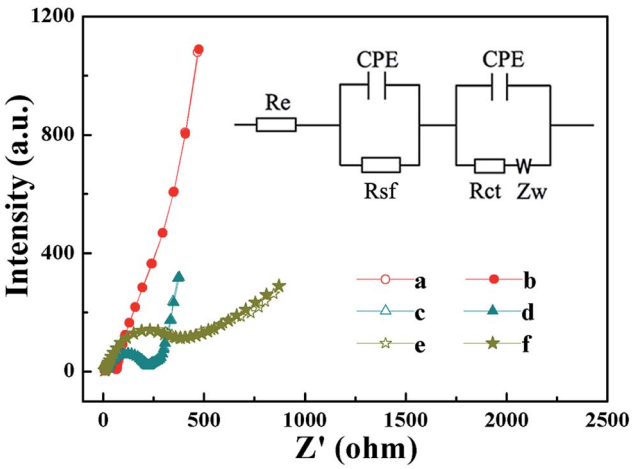

Fig. 8 The experimental Nyquist plots of (a) the MWNTs, (c) Fe_3O_4–MWNTs (1 : 3) and (e) Fe_3O_4–MWNTs (1 : 1). The fitted Nyquist plots of (b) the MWNTs, (d) Fe_3O_4–MWNTs (1 : 3) and (f) Fe_3O_4–MWNTs (1 : 1). The inset is the corresponding equivalent circuit.

nanocomposites and accommodates the large volume changes during the lithiation/delithiation processes;[67] (2) the structure of well-dispersed Fe_3O_4 nanoparticles anchored on MWNTs effectively prevents the aggregation of Fe_3O_4 nanoparticles; (3) the small size of Fe_3O_4 nanoparticles (*ca.* 10–20 nm) and the thin walls of MWNTs facilitate the ions diffusion in the electrode and increase the contact surface between the active materials and electrolyte; and (4) the good contact between Fe_3O_4 nanoparticles and MWNTs has stabilized the structure of the nanocomposites during the charge/discharge process.

4. Conclusions

Uniform distribution of Fe_3O_4 nanoparticles homogenously anchored on MWNTs were fabricated by a novel hydrothermal method in methanol–glycerol solvent followed by an annealing process in argon atmosphere. The Fe_3O_4/MWNTs nanocomposites exhibited superior cycling performance (829 mA h g^{-1} after 50 cycles at a current density of 100 mA g^{-1}) and rate performance (686, 624, 541, 408, and 294 mA h g^{-1} at 200, 400, 800, 1600, and 3200 mA g^{-1}, respectively). The fascinating electrochemical performances originate from the network of MWNTs in the nanocomposites as well as the high capacity from nano-sized Fe_3O_4 particles. The incorporation of the conductive MWNTs with transition metal oxides is proved to be a promising way to make anode materials with superior electrode performance.

Acknowledgements

This work was supported by the Independent Innovation Foundations of Shandong University (2012ZD001, 2012JC013). The authors also acknowledge the financial supports from the Doctoral Program of Higher Education of China (20130131110068), New Century Excellent Talent Program (NCET-10-0545), State Education Ministry, and Natural Science Fund for Distinguished Young Scholars of Shandong (JQ201312). Z. Guo appreciates the support from National Science Foundation (NSF, CMMI 10-30755 and CMMI 13-14486) USA.

References

1 J. Maier, *Nat. Mater.*, 2005, **4**, 805–815.
2 J. M. Tarascon and M. Armand, *Nature*, 2001, **414**, 359–367.
3 S. M. Abbas, S. T. Hussain, S. Ali, N. Ahmad, N. Ali and K. S. Munawar, *Electrochim. Acta*, 2013, **105**, 481–488.
4 G. Lu, S. Qiu, J. Liu, X. Wang, C. He and Y. Bai, *Electrochim. Acta*, 2014, **117**, 230–238.
5 S. Hwang, G. Kim, S. Yun and K. Ryu, *Electrochim. Acta*, 2012, **78**, 406–411.
6 X. H. Huang, J. P. Tu, X. H. Xia, X. L. Wang, J. Y. Xiang, L. Zhang and Y. Zhou, *J. Power Sources*, 2009, **188**, 588–591.
7 D. Qiu, B. Zhao, Z. Lin, L. Pu, L. Pan and Y. Shi, *Mater. Lett.*, 2013, **105**, 242–245.
8 Y. Cai, S. Liu, X. Yin, Q. Hao, M. Zhang and T. Wang, *Phys. E*, 2010, **43**, 70–75.
9 S. Chen, F. Liu, Q. Xiang, X. Feng and G. Qiu, *Electrochim. Acta*, 2013, **106**, 360–371.
10 W. Yue, S. Tao, J. Fu, Z. Gao and Y. Ren, *Carbon*, 2013, **65**, 97–104.
11 J. Hu, H. Li, X. Huang and L. Chen, *Solid State Ionics*, 2006, **177**, 2791–2799.
12 B. Guo, M. Chi, X. Sun and S. Dai, *J. Power Sources*, 2012, **205**, 495–499.
13 C. Chen, N. Ding, L. Wang, Y. Yu and I. Lieberwirth, *J. Power Sources*, 2009, **189**, 552–556.
14 Z. Cui, L. Hang, W. Song and Y. Guo, *Chem. Mater.*, 2009, **21**, 1162–1166.
15 C. Chang, J. Tseng, J. Horng and C. Shu, *Compos. Sci. Technol.*, 2008, **68**, 2954–2959.
16 L. Hu, Y. Sun, F. Zhang and Q. Chen, *J. Alloys Compd.*, 2013, **576**, 86–92.
17 W. Zhang, X. Wang, H. Zhou, J. Chen and X. Zhang, *J. Alloys Compd.*, 2012, **521**, 39–44.
18 A. L. M. Reddy, M. M. Shaijumon, S. R. Gowda and P. M. Ajayan, *Nano Lett.*, 2009, **9**, 1002–1006.
19 Y. Wang, H. C. Zeng and J. Y. Lee, *Adv. Mater.*, 2006, **18**, 645.
20 P. Poizot, S. Laruelle, S. Grugeon, L. Dupont and J. M. Tarascon, *Nature*, 2000, **407**, 496–499.
21 S. K. Behera, *J. Power Sources*, 2011, **196**, 8669–8674.
22 M. K. Kim, B. Y. Jang, J. S. Lee, J. S. Kim and S. Nahm, *J. Power Sources*, 2013, **244**, 115–121.
23 A. S. Arico, P. Bruce, B. Scrosati, J. M. Tarascon and W. Van Schalkwijk, *Nat. Mater.*, 2005, **4**, 366–377.
24 Y. Chen, B. Song, L. Lu and J. Xue, *Nanoscale*, 2013, **5**, 6797.
25 D. Wang, D. Choi, J. Li, Z. Yang, Z. Nie, R. Kou, D. Hu, C. Wang, L. V. Saraf, J. Zhang, I. A. Aksay and J. Liu, *ACS Nano*, 2009, **3**, 907–914.
26 A. K. Rai, J. Gim, T. A. Ly and J. Kim, *Electrochim. Acta*, 2013, **100**, 63–71.
27 Y. J. Mai, J. P. Tu, C. D. Gu and X. L. Wang, *J. Power Sources*, 2012, **209**, 1–6.
28 M. Z. Kassaee, E. Motamedi and M. Majdi, *Chem. Eng. J.*, 2011, **172**, 540–549.
29 W. Zhang, B. Xu and L. Jiang, *J. Mater. Chem.*, 2010, **20**, 6383–6391.
30 Y. Sun, Q. Wu and G. Shi, *Energy Environ. Sci.*, 2011, **4**, 1113–1132.
31 J. Wang, R. Ran, M. O. Tade and Z. Shao, *J. Power Sources*, 2014, **254**, 18–28.
32 R. Epur, M. K. Datta and P. N. Kumta, *Electrochim. Acta*, 2012, **85**, 680–684.
33 D. Ahn, X. Xiao, Y. Li, A. K. Sachdev, H. W. Park, A. Yu and Z. Chen, *J. Power Sources*, 2012, **212**, 66–72.
34 Y. Zhong, G. Li, S. Liu, M. Zhong, H. Wang and H. Li, *J. Optoelectron. Adv. Mater.*, 2012, **3–4**, 245–250.
35 C. Wu, Q. Zhuang, Y. Wu, L. Tian, Y. Cui and X. Zhang, *Mater. Lett.*, 2013, **113**, 1–4.
36 J. Wang, C. Zhong, D. Wexler, N. H. Idris, Z. Wang, L. Chen and H. Liu, *Chem.–Eur. J.*, 2011, **17**, 661–667.
37 D. Chen, G. Ji, Y. Ma, J. Y. Lee and J. Lu, *ACS Appl. Mater. Interfaces*, 2011, **3**, 3078–3083.

38 Y. Chen, H. Xia, L. Lu and J. Xue, *J. Mater. Chem.*, 2012, **22**, 5006–5012.
39 X. Wang, Z. Zhao, J. Qu, Z. Wang and J. Qiu, *J. Phys. Chem. Solids*, 2010, **71**, 673–676.
40 Y. Cheng, Y. Liu, J. Huang, K. Li, Y. Xian, W. Zhang and L. Jin, *Electrochim. Acta*, 2009, **54**, 2588–2594.
41 D. Shi, J. P. Cheng, F. Liu and X. B. Zhang, *J. Alloys Compd.*, 2010, **502**, 365–370.
42 D. Guan, Z. Gao, W. Yang, J. Wang, Y. Yuan, B. Wang, M. Zhang and L. Liu, *Mater. Sci. Eng., B*, 2013, **178**, 736–743.
43 S. Wang, H. Bao, P. Yang and G. Chen, *Anal. Chim. Acta*, 2008, **612**, 182–189.
44 J. Sui, J. Li, Z. Li and W. Cai, *Mater. Chem. Phys.*, 2012, **134**, 229–234.
45 I. H. Park, M. Christy, P. Kim and K. S. Nahm, *Mater. Sci. Eng., B*, 2014, **58**, 75–80.
46 Y. He, L. Huang, J. Cai, X. Zheng and S. Sun, *Electrochim. Acta*, 2010, **55**, 1140–1144.
47 Q. Guo, P. Guo, J. Li, H. Yin, J. Liu, F. Xiao, D. Shen and N. Li, *J. Solid State Chem.*, 2014, **213**, 104–109.
48 G. Wang, X. Shen, J. Yao, D. Wexler and J. Ahn, *Electrochem. Commun.*, 2009, **11**, 546–549.
49 J. Zhu, M. Chen, H. Qu, X. Zhang, H. Wei, Z. Luo, H. A. Colorado, S. Wei and Z. Guo, *Polymer*, 2012, **53**, 5953–5964.
50 H. Gu, H. Wei, J. Guo, N. Haldolaarachige, D. P. Young, S. Wei and Z. Guo, *Polymer*, 2013, **54**, 5974–5985.
51 H. Gu, S. B. Rapole, J. Sharma, Y. Huang, D. Cao, H. A. Colorado, Z. Luo, N. Haldolaarachchige, D. P. Young, B. Walters, S. Wei and Z. Guo, *RSC Adv.*, 2012, **2**, 11007–11018.
52 H. Zhang and G. Zhu, *Appl. Surf. Sci.*, 2012, **258**, 4952–4959.
53 F. Wu, R. Huang, D. Mu, X. Shen and B. Wu, *J. Alloys Compd.*, 2014, **585**, 783–789.
54 Q. Zhang, Z. Shi, Y. Deng, J. Zheng, G. Liu and G. Chen, *J. Power Sources*, 2012, **197**, 305–309.
55 S. K. Behera, *J. Power Sources*, 2011, **196**, 8669–8674.
56 S. Wang, J. Zhang and C. Chen, *J. Power Sources*, 2010, **195**, 5379–5381.
57 Y. Yu, Y. Zhu, H. Gong, Y. Ma, X. Zhang, N. Li and Y. Qian, *Electrochim. Acta*, 2012, **83**, 53–58.
58 J. Feng, S. Xiong, Y. Qian and L. Yin, *Electrochim. Acta*, 2014, **129**, 107–112.
59 Y. Deng, Q. Zhang, Z. Shi, L. Han, F. Peng and G. Chen, *Electrochim. Acta*, 2012, **76**, 495–503.
60 J. Xu and Y. Zhu, *ACS Appl. Mater. Interfaces*, 2012, **4**, 4752–4757.
61 S. Laruelle, S. Grugeon, P. Poizot, M. Dolle, L. Dupont and J. M. Tarascon, *J. Electrochem. Soc.*, 2002, **149**, A627–A634.
62 X. Li, L. Qiao, D. Li, X. Wang, W. Xie and D. He, *J. Mater. Chem. A*, 2013, **1**, 6400–6406.
63 C. Gong, Y. Bai, Y. Qi, N. Lun and J. Feng, *Electrochim. Acta*, 2013, **90**, 119–127.
64 J. K. Feng, M. O. Lai and L. Lu, *Electrochim. Acta*, 2012, **62**, 103–108.
65 M. V. Reddy, T. Yu, C. Sow, Z. X. Shen, C. T. Lim, G. V. S. Rao and B. V. R. Chowdari, *Adv. Funct. Mater.*, 2007, **17**, 2792–2799.
66 H. Zhang, H. Song, X. Chen, J. Zhou and H. Zhang, *Electrochim. Acta*, 2012, **59**, 160–167.
67 J. Li, D. Le, P. P. Ferguson and J. R. Dahn, *Electrochim. Acta*, 2010, **55**, 2991–2995.
68 Z. Liu, R. Guo, G. Li, Q. Bu, W. Zhao and Y. Tong, *Electrochim. Acta*, 2012, **59**, 449–454.